Journal of Asian Earth Sciences: X 1 (2019) 100006

Contents lists available at ScienceDirect

Journal of Asian Earth Sciences: X

journal homepage: www.journals.elsevier.com/journal-of-asian-earth-sciences-x

Fragments of asthenosphere incorporated in the lithospheric mantle underneath the Subei Basin, eastern China: Constraints from geothermobarometric results and water contents of peridotite xenoliths in Cenozoic basalts

Yan-Tao Hao[a,*], Costanza Bonadiman[b,*], Massimo Coltorti[b], Qun-Ke Xia[a]

[a] School of Earth and Space Sciences, Zhejiang University, Hangzhou 310027, China
[b] Department of Physics and Earth Sciences, University of Ferrara, Via Saragat 1, 44121 Ferrara, Italy

ARTICLE INFO

Keywords:
Water contents
Fertile mantle
Melting models
Water diffusion
Asthenosphere/lithosphere

ABSTRACT

Anhydrous, medium/coarse-grained spinel bearing mantle xenoliths from the Subei Basin, Eastern China have mineral arrangements that reflect low energy geometry. Because of clinopyroxene modal contents, they are grouped into cpx-rich lherzolites (cpx ≥ 14percentage), lherzolites (8 < cpx < 14%), cpx-poor lherzolites (6 < cpx ≤ 8%) and harzburgites (cpx up to 4%), without relevant textural differences from the most fertile to the most depleted lithotypes. The cpx-rich lherzolites have mineral chemistry close in composition to Primitive Mantle (PM), whereas cpx-poor lherzolite (and lherzolite) and harzburgite groups cannot be considered as a result of direct melting of the PM source. In addition, the high LREE, Th and U contents, coupled with a Sr enrichment of clinopyroxenes in these lithotypes, indicate the circulation of a silicate melt (with crustal components) in a variably depleted mantle sector well before the entrapment of the xenoliths by the host basalt.

Despite the large differences in refractory lithophile element contents (i.e. Ca, Al and REE), the equilibrium temperatures never exceed 1021 °C with a constant difference (< 200 °C) from harzburgites to cpx-rich lherzolites. Measured mineral water contents indicate that the whole rock contains, on average, 19 ± 7 ppm of H_2O without any systematic variation among rock types nor correlation with Al_2O_3, light-REE and Yb (or Y) contents of cpx. The cpx H_2O contents of cpx-rich lherzolites (41–96 ppm) are, on average, one order of magnitude lower than those theoretically expected (214–530 ppm) for a residuum after a maximum of 3% of PM fractional (≈ bulk) melting in the spinel stability field.

The proposed dehydration model suggests that the cold highly refractory harzburgites and cpx-poor lherzolites (and lherzolites?) may represent old cratonic lithospheric mantle modified at depth by the interaction with silicate melts, which may also have involved crustal components. In turn, cpx-rich lherzolites constitute fragments of upwelling fertile asthenosphere, which caused the removal/erosion of the lowermost part of the lithospheric mantle. This asthenosphere portion may have been incorporated in the lithospheric region since the Jurassic and it may have progressively cooled down after one (or more) partial melting episodes. The water depletion can be accounted for a continuous loss by diffusion during the subsolidus chemical-physical readjustment, well after (> 5My, based on modelled H_2O solid-solid diffusion rate) the occurrence of the last melting episode.

1. Introduction

The North China Craton (NCC), characterized by crustal remnants older than 3.8 Ga (Liu et al., 1992), represents a unique large craton of eastern Eurasia and its formation and subsequent evolution are well preserved in the Phanerozoic geology of eastern China. In recent years, geological, geophysical and geochemical studies have converged to suggest that the Eastern Block of the North China Craton (NCC) has lost > 100 km in thickness of its lithospheric root (Windley et al., 2010; Menzies et al., 2007 and references therein). However, currently the subject of debate, is how and when the Archaean sub-continental lithospheric mantle was delaminated/thinned (e.g. Griffin et al., 1998, 2009; Xu, 2001; Zhang et al., 2003; Rudnick et al., 2004; Wu et al., 2006; Deng et al., 2004; Gao et al., 2004; Ying et al., 2013; Tang et al.,

* Corresponding authors.
E-mail addresses: ythao@zju.edu.cn (Y.-T. Hao), bdc@unife.it (C. Bonadiman).

https://doi.org/10.1016/j.jaesx.2019.100006
Received 5 September 2018; Received in revised form 26 December 2018; Accepted 12 January 2019
Available online 23 January 2019

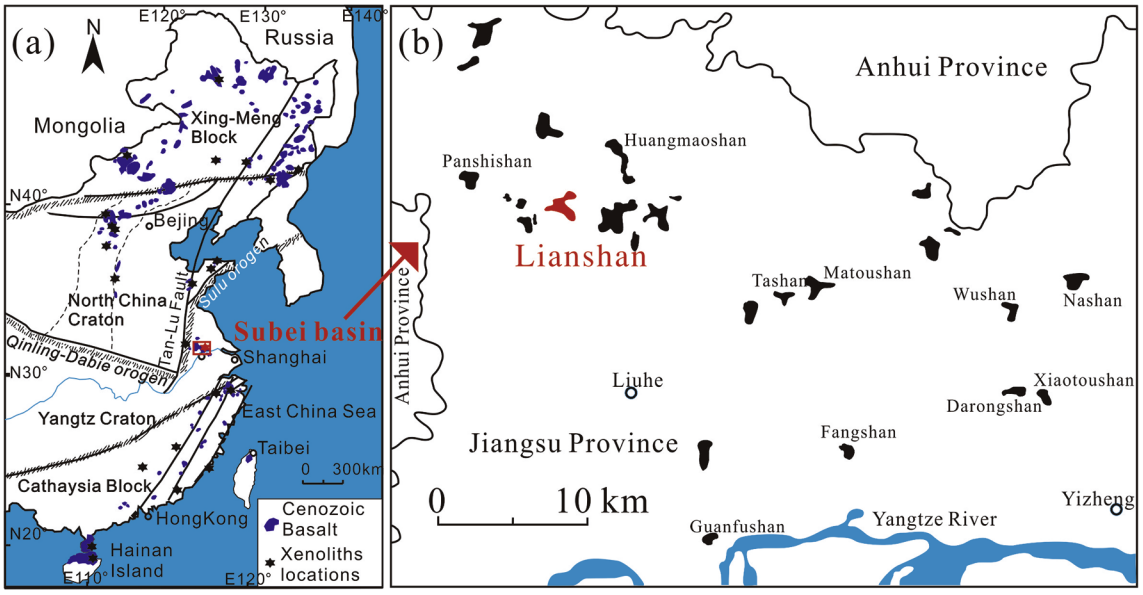

Fig. 1. Simplified map of Eastern China (a) main tectonic lines separating the actual lithospheric blocks (after Xia et al., 2010) and location of the Subei Basin. (b) distribution of the Subei Basin Cenozoic mantle xenolith bearing volcanism; in red, the LS sample locality of this study. (For interpretation of the references to color in this figure legend, the reader is referred to the web version of this article.)

2013; Chen et al., 2016; Wu et al., 2017). Present day models can be broadly grouped into "top-down" or "bottom-up" models. The top–down delamination models imply rapid removal (less than 5 Ma) of the entire sub-continental lithospheric mantle, including parts of the lower crust (Gao et al., 2004, 2008); whereas the bottom-up thermal/chemical erosion models imply a protracted up to ~100 Ma lithospheric thinning. However, low water contents in the nominally anhydrous minerals of peridotite xenoliths (Bonadiman et al., 2009) from the eastern part of the NCC have been initially interpreted as the presence of ancient lithospheric mantle's relicts, rather than a juvenile accreted asthenospheric mantle (Xia et al., 2010; Hao et al., 2012).

One critical line of investigation that may be used to address the questions regarding the nature and evolution of the sub-continental lithospheric mantle of the NCC is to examine the mantle-derived peridotite xenoliths. In fact, the majority of peridotite xenoliths, which formed in the sub-continental lithospheric mantle, are rapidly transported to the surface, along with their host magmas, in a matter of few hours/days. Thus, they represent snapshots of the sub-continental lithospheric mantle and have the great potential of unravelling the nature and evolution of their source. The Subei basin occupies a critical position at the southern edge of the NCC and is located within the collision zone between the NCC and the South China Block (SCB), with a northward-directed subduction (Li, 1994; Chung, 1999). Consequently, the peridotite xenoliths from the Subei basin have the potential to reveal not only the nature of the sub-continental lithospheric mantle and their possible relationship with the asthenosphere, but also to shed light on the metasomatic processes associated with subduction.

In this paper, with obtained new trace element data of clinopyroxene (cpx), we characterize the mantle domain beneath the Subei basin, eastern China, through a detailed geochemical study of peridotite xenoliths hosted by the Cenozoic basalts from Lianshan (LS). The major and trace element chemistry (including H_2O) of peridotite minerals provides a coherent petrological history of this geodynamically complex region.

2. Geological background

The geological architecture of the eastern part of China resulted from the amalgamation of two large tectonic blocks, the NCC and the SCB. The latter can be divided into the Yangtze block to the northwest and the Cathaysia block to the southeast. The NCC is separated from the Xing-Meng Block by the Central Asia Orogen to the north and from the Yangtze block by the Triassic Qinling-Dabie orogen to the south. A continental scale Tan-Lu fault cuts both the Xing-Meng block and the NCC. The eastern part of NCC experienced widespread lithospheric thinning and evolved from a thick (~200 km), cold (~40 mW/m^2) and highly refractory lithospheric mantle in the mid-Ordovician to a thin (60–80 km), hot (60–80 mW/m^2) and fertile lithospheric mantle after the late Mesozoic (Menzies et al., 2007, and references therein).

From Early Triassic to Late Jurassic, the SCB and the NCC converged, forming the Qinling-Dabie-Sulu orogen and a large ultra-high pressure suture zone (e.g., Li et al., 1993). This was transected during middle Triassic to early Cretaceous by the Tan-Lu sinistral strike slip fault, which moved the Sulu orogeny northward (Zhu et al., 2009). The superficial tectonics indicates that the suture between the SCB and the NCC eastward of the fault is placed slightly north of the Sulu terrain. However, based on linear aeromagnetic anomalies, deep seismic profiles and regional geology, Li (1994) proposed a crustal detachment model. This model postulates that during the mid-Mesozoic a collision between the two continental blocks occurred: the upper crust of the SCB in the Subei Basin-Yellow Sea region was detached from the lower crust and thrust over the NCC for more than 400 km, whereas the lower part of the lithosphere was subducted under the NCC along a subsurface suture located east of Nanjing (Fig. 1). Recently, Su et al. (2013) proposed a similar subsurface boundary, based on the study of Sr–Nd–Pb–Hf isotopic systems of Cretaceous granitic plutons. The Subei basin is located east of Tanlu fault, just north of the proposed subsurface suture. It is still unclear whether the mantle lithospheric roots beneath the Subei basin belong to the NCC or the SCB.

The Subei basin experienced widespread Cenozoic volcanism, which can be either directly or indirectly related to the lithospheric thinning of the NCC. The volcanism includes minor tholeiitic products mainly erupted during the early Paleogene, and xenolith-bearing alkali basalts extensively erupted during the Neogene (Fig. 1). The integration of sulfide and whole-rock Re–Os data suggests that the oldest part of the lithospheric mantle sampled by the peridotite xenoliths beneath Subei basin may be Paleoproterozoic in age, and subsequently modified during Mesoproterozoic and Phanerozoic times (Reisberg et al., 2005; Xu et al., 2008).

The studied peridotite xenoliths are from Lianshan in the Subei

basin, located in northwestern Jiangsu Province (Fig. 1) and are contained in the alkali basalts of the Huanggang volcanic group, dated between 10 and 12 Ma (Shao et al., 1989).

3. Material and analytical methods

3.1. Petrography and modal composition

The LS sample collection is entirely constituted by spinel-bearing peridotite without any evidence of hydrous phase. Twenty-two samples out of about forty xenoliths were selected for this study, based on xenolith size and representativeness of the different lithology. They range in size from 5 to 10 cm and do not show any evidence of alteration or host basalt infiltration.

As the thin section includes just a small amount of the xenoliths in relation to the grain size, mass balance calculations between whole rock and mineral major element compositions are generally preferred in determining modal percentages of the minerals. However, for the LS xenoliths, whole rock analyses were possible for seven samples only, thus the mineral proportions of all samples were estimated by thin section point counting (Table 1). This method can be confidently applied, since the grains are all < 3 mm in size; because of the good match between the two methods observed for seven samples, we felt confident in classifying the entire sample collection by point counting.

The majority of the samples are lherzolites. The samples can be subdivided in three groups depending on the clinopyroxene (cpx) modal contents: cpx-poor lherzolites (6 < cpx ≤ 8%), lherzolites (8 < cpx < 14%) and cpx-rich lherzolites (cpx ≥ 14%, with LS04 being the most fertile with up to 18% cpx) and harzburgites (up to 4% cpx). This last group is represented by only two samples (LS26 and LS16).

According to Mercier and Nicolas (1975), the most common texture shown by the LS xenolith population is the protogranular type and, generally, they do not show any pronounced fabric orientation. No hydrous phases, nor metasomatic textures, glassy patches and sieved-spongy crystals were observed. The peridotite samples are textually remarkably different from those studied by Lu et al. (2013) and sampled in the same area; the latter have dominantly "porphyroclastic fine-grained microstructures" and evident superimposed metasomatic textures (i.e.: spongy cpx, containing CO_2 fluid inclusions and secondary minerals). Relatively coarse olivine and orthopyroxene (opx) grains (3–5 mm) show curvilinear crystal boundaries. Due to strain, the crystals may be polygonized in medium-grained substructure, with evidence of recrystallization (LS06, Fig. 2) from a previous coarse-grained assemblage (LS17, Fig. 2). Large grains of olivine in almost all samples show kink banding. The orthopyroxenes do not show evident degree of deformation, they are texturally homogeneous except for the samples LS01 and LS31, where the grains are particularly coarse (up to 5 mm) and exsolved fine lamellae of cpx were observed (LS31; Fig. 2). Clinopyroxene and spinel occur as fairly smaller grains (< 3 mm) and blebs either within orthopyroxene or in contact with it (LS26; Fig. 2). In samples LS01, LS06 and LS23, the spinel is anomalously large (up to 4 mm), sometimes aligned and with the typical "holly-leaf" outline. No relevant textural differences were observed from the most fertile to the most refractory lithotype.

3.2. Analytical techniques

Trace element compositions of cpx were obtained by LA-ICP-MS on separate grains fixed in epoxy mounts at the University of Science and Technology of China. Mineral grains were ablated in situ with GeoLas pro ArF excimer laser system with beam wavelength 193 nm at 10 Hz repetition rate and 10 J/cm^2 energy per pulse. The ablation crater diameters were about 60 μm in size and the sample aerosol was carried to PerkinElmer DRCII ICP-MS by high purity Helium with flow rate of 0.3 L/min. The analysis consists of 80–100 replicates within 80–100 s and was processed by LaTEcalc software. The commercial software GLITTER 4.0 (Macquarie University; Griffin et al., 2008) was used for data reduction with NIST 610 silicate glass as external standard and ^{44}Ca as the internal standard using values for CaO from the electron microprobe analyses for clinopyroxene. USGS glass BCR-2G was measured as an unknown in every session as quality control and always yielded values within 10% of the published values. Despite the general primary protogranular characters of all the lithotypes, in any case care was taken to analyze only unaltered grain areas, which was an issue with the clinopyroxenes. Prior to each spot analysis the target area was checked in reflected and in transmitted light to ensure clear, crack-free and unaltered spots. The time-resolved signals for each individual analysis were screened for inclusions or cracks (identified by spikes in the time-resolved signal) and affected areas or complete analyses were discarded accordingly.

Major element compositions of LS peridotite minerals were determined using a JEOL Superprobe (JXA 8100) at Nanjing University (China). Detection limits were generally between 0.01 and 0.07 wt%. The operating accelerating voltage was 15 kV and 20 nA and 10 to 20 s counting time for all phases; the beam size was 2 μm. Natural minerals and synthetic oxides were used as standards for calibrations. ZAF procedure was used for data correction.

4. Results

4.1. Mineral chemistry

The average values of major elements for olivine, cpx, opx and spinel. of most LS peridotites are reported in Xia et al. (2010, in Tables 1–4). In the paper, we report the detail analysis of spots for each minerals in Table S1.

4.1.1. Olivine, orthopyroxene and spinel

Olivine shows in all groups the same textural features and within individual sample has similar inter-grain compositions. Mg# (Mg^{2+}/(Mg^{2+} + Fe^{2+}) *100, all Fe was assumed as Fe^{2+}) values range from 89.15 (lherzolites, LS22) to 91.90 (harzburgite, LS16). NiO contents vary from 0.21 to 0.48 wt% (weight percent), with, on average, a positive correlation with Mg#. The majority of samples are coherent with the Ni contents of residual olivine after the extraction of partial melts (e.g. Mysen, 1978). Olivine from spinel peridotites typically has 0.31–0.43 wt% of NiO, with an average value of 0.37 wt% (Korenaga and Kelemen, 2000). The NiO contents for Primitive Mantle (PM) olivine are 0.28–0.30 wt%. In this range fall the great majority of olivine from cpx-rich lherzolites (Fig. 3).

Orthopyroxene in lherzolites groups and harzburgite shows restricted inter-grain compositional variations. Mg# values vary between 89.44 (lherzolites LS22) and 92.44 (harzburgite LS16); Al_2O_3 contents range from 1.63 wt% (harzburgite LS16) to 4.65 wt% (cpx-rich lherzolites LS04), showing a negative correlation with Mg# (Fig. 4). Interesting to note, LS opx in cpx-rich lherzolites are all < 4.65 wt% Al_2O_3 contents, in spite of any Mg# values variation (Fig. 4a). An ideal negative correlation between Al_2O_3 contents and Mg# are observed. Opx shows low to very low TiO_2 contents (< 0.2 wt%), which decrease with increasing Mg# (Fig. 4b). The low CaO contents (< 0.71 wt%) show no correlation with Mg#, but are roughly correlated with Na_2O contents (< 0.18 wt%).

Spinel grains from individual samples are homogeneous within analytical error, with less than 10% intra-grain compositional variations for Cr# (Cr/(Cr + Al)*100) and Mg#. They vary from 10.48 to 49.03 and 66.16 to 79.77, respectively. These two ratios show the usual negative correlation similar to residual abyssal, plagioclase-free peridotite (Dick and Bullen, 1984). TiO_2 contents are less than 0.15 wt% and, just in harzburgite LS26 up to 0.27 wt%. Moreover, the correlation of spinels from cpx-rich lherzolites (LS 23) and lherzolites (LS22, LS20, LS06; LS05), with the bulk rock composition (Al_2O_3 = 1.72–3.37 wt%; TiO_2 = 0.06–0.16 wt%) is consistent with variable extents of PM melt

Table 1
Mineral modal, temperature and oxygen fucaity estimate of Lianshan peridotites and summary of geochemical parameters.

Sample	rock type	Mode (%) point counting				Mode (%) mass balance				WR Mg#	Mg# ol	Temperature		Δlog fO2	OH (ppm wt)		
		ol	opx	cpx	sp	ol	opx	cpx	sp			T_{BKN}(opx-cpx)	T_{NWB}(ol-sp)	Ballhaus	CPX*	OPX*	WR**
LS16	hz	75	19	4	2						91.83	833***	883	−1.1			
LS26	hz	72	20	4	4						90.93	837	907	−0.8	57	19	11
LS03	cpx-poor lh	72	20	6	2	70	20	8	2	91.13***	91.47	941	905	−0.5	41	17	9
LS12	cpx-poor lh	74	15	8	3						91.75	916	925	−0.2	78	32	17
LS15	cpx-poor lh	69	21	7	3						91.32	858	908	−1.3			
LS17	cpx-poor lh	73	18	8	1	75	16	7	1	93.75***	91.74	884	1012	−0.6	37	17	9
LS19	cpx-poor lh	66	26	7	1						90.52	856	932	−1.2	89	45	24
LS21	cpx-poor lh	78	13	6	3						91.49	895	894	−1.6		16	0
LS01	lh	55	28	12	5						90.09	849	929	−1.1	55	18	15
LS05	lh	56	29	13	2	60	28	11	1	91.10***	90.37	810	998	−0.7	90	34	27
LS06	lh	60	26	11	3	65	24	10	2	91.98***	89.84	969	1021	−1.3	73	32	21
LS08	lh	66	20	10	4						90.13	888	973	−1.0	42	15	10
LS09	lh	65	20	11	4						90.30	802	911	−1.2			
LS20	lh	74	14	11	1	79	10	10	1	93.27***	90.33	1015	876	−1.7	84	34	20
LS22	lh	59	26	13	2	63	24	12	2	90.57***	89.23	903	930	−1.6	102	41	31
LS30	lh	62	24	12	2						89.84	970	917	−2.0	92	29	24
LS02	cpx-rich lh	52	30	14	4						89.79	890	982	−1.8	41	13	12
LS04	cpx-rich lh	50	29	18	3						89.55	1001	1004	−0.9	56	28	22
LS07	cpx-rich lh	57	27	14	2						89.97	970	988	−1.3	96	30	28
LS23	cpx-rich lh	60	24	14	2	62	22	15	2	91.42***	89.71	1014	875	−2.2	73	32	23
LS24	cpx-rich lh	45	34	17	4						89.89	968	1013	−1.2	80	34	30
LS31	cpx-rich lh	53	27	17	3						89.32	829	940	−1.1	55	16	17
average	hz										91.38 ± 0.45	835 ± 2	895 ± 12	−1.0 ± 0.2	57	19	11
	cpx-poor lh										91.38 ± 0.86	891 ± 36	929 ± 36	−0.9 ± 0.7	61 ± 24	25 ± 9	15 ± 6
	lh										90.02 ± 0.79	901 ± 39	944 ± 68	−1.3 ± 0.7	77 ± 35	29 ± 11	21 ± 11
	cpx-rich lh										89.70 ± 0.38	945 ± 116	967 ± 92	−1.4 ± 0.8	67 ± 26	26 ± 13	22 ± 10

* Data from Bonadimann et al. (2009).
** Data from Xia et al. (2010).
*** Whole rock X-ray Florescence (XRF) analyses on a pressed powder dish were carried out at the Department of Physics and Earth Science, University of Ferrara, on advant-X Thermo ARL mass balance: see text for full description.

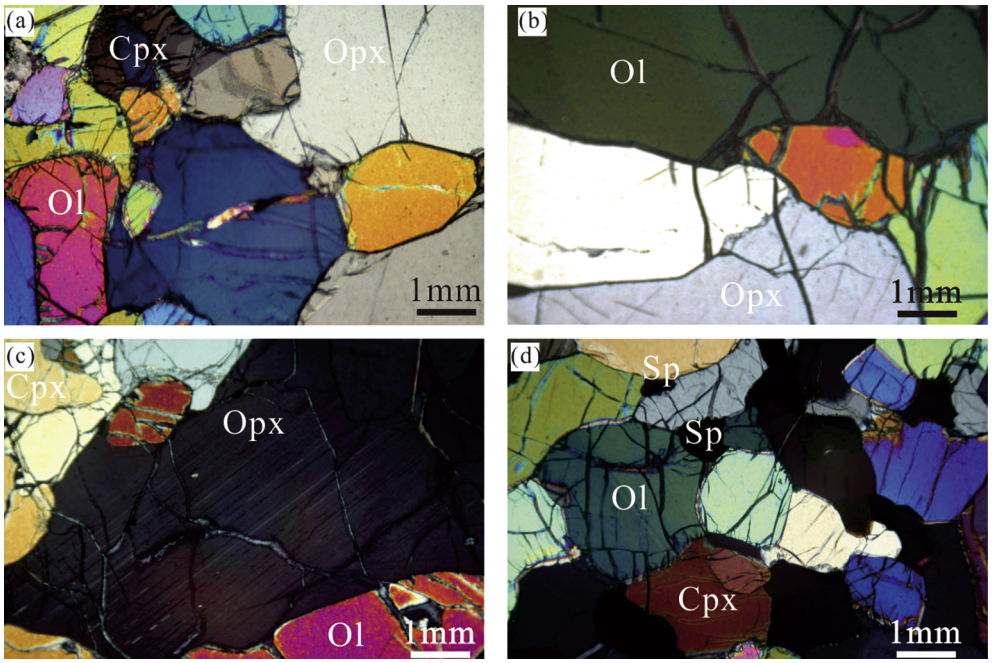

Fig. 2. Cross polarized light photomicrographs of LS xenoliths illustrating the petrographic features of the four lithoptypes. (a) medium/coarse grained lherzolites LS16 showing polygonized cpx, olivine and opx grains; (b) coarse-grained mineral assemblage of the cpx-poor lherzolites LS17- scale as in (a); (c) exsolved fine lamellae of cpx in opx in cpx-rich lherzolites LS31- scale as in (a); (d) medium grained harzburgite LS16 with cpx and spinel reflecting low energy geometry.

depletion (Workman and Hart, 2005; Craddock et al., 2013). Spinels from cpx-rich lherzolites are analog to the most fertile spinel of the abyssal field (Craddock et al., 2013).

4.1.2. Clinopyroxene

Clinopyroxene in LS xenoliths displays a textural equilibrium with opx, but reflects a larger intra-grain zonation for FeO contents, sensitively affecting Mg# (i.e. lherzolites LS22, (Fig. 5). On average Mg# varies between 89.59 (cpx-rich lherzolites LS04) and 94.07 (harzburgite LS16). By contrast, TiO_2 and Al_2O_3 contents are very homogeneous among grains of the same sample. Both oxides show a negative correlation with Mg#, with Al_2O_3 contents varying from 7.15 to 1.73 wt% and TiO_2 from 0.79 wt% to detection limit (Fig. 5a and b). The Al_2O_3 contents in cpx-rich lherzolites do not exceed a cpx value of 7.15 wt%. Na_2O contents follow the same geochemical behavior of Al_2O_3, being buffered at 2.0 wt% in cpx-rich lherzolites (Fig. 5c). This indicates that, at least for the most "fertile" LS lherzolites, the Al_2O_3 (and Na_2O) contents result saturated by the bulk peridotite system. In cpx-rich lherzolites, cpx-poor lherzolites LS21 and harzburgite LS16, Na_2O is constant at 1.47–1.99 wt %, independent of Mg# values (Fig. 5c). On the other hand, for lherzolites, cpx-poor lherzolites and harzburgite LS26, Na_2O contents systematically decrease (down to 0.12 wt%) with increasing Mg#.

Clinopyroxene is the most important phase hosting trace element in anhydrous spinel peridotites. In the majority of LS peridotite xenoliths, the differences between individual analyses of the same mineral are within analytical error, except for LS08 and LS30, which show some heterogeneity in Light Rare Earth Elements LREE (Table 2).

Fig. 6a and b shows REE and incompatible trace element distributions of harzburgite and cpx-poor lherzolites groups. Harzburgite LS16 shows a highly enriched REE pattern from Er to light (L) REE with La about 40 times chondrite and $(La/Yb)_{Ch}$ = 10.8). The sample presents strong Ti and Zr negative anomalies (Ti* = 0.33, Ti* = 2 × Ti_{PM}/(Eu_{PM} + Gd_{PM}) and Zr* = 0.64, Zr* = 2 × Zr_{PM}/(Nd_{PM} + Sm_{PM}), a feeble Sr positive anomaly (Sr* = 1.85, Sr* = 2 × Sr_{PM}/(Pr_{PM} + Nd_{PM}) and, together with the cpx-poor lherzolites LS15 and LS17. It presents the highest contents of Th and U (15 and 20 times primitive mantle value respectively) of the entire LS xenolith population. By contrast, the other harzburgite (LS26) shows the lowest trace elements (including REE) contents. This sample is characterized by flat REE pattern with $(La/Yb)_{Ch}$ about 0.80 and $(Sm/Yb)_{Ch}$ about 0.6, with Ti, Zr and Sr, which mimic the same anomalies observed in harzburgite LS16 (Ti* = 0.32, Zr* = 0.41 and Sr* = 1.56). Despite the well-equilibrated textural types, cpx in cpx-poor lherzolites and lherzolites groups records extremely heterogeneous intergroup incompatible trace element contents and distributions (Fig. 6a, b, c and d). On the other hand, the five cpx-rich lherzolites show almost identical REE and incompatible trace element profiles (Fig. 6e and f, respectively). Cpx in cpx-poor lherzolites records variable degrees of depletion, with Yb_{Ch} varying from 3.3 to 6.4 (Fig. 6a). Four samples out of six show positive fractionated REE patterns (Fig. 6a, $(La/Yb)_{Ch}$ = 3.25–18.82) and high Th and U contents (Th_{PM} = 6.82–55.17 and U_{PM} = 8.41–24.07; Fig. 6b). Conversely, cpx-poor lherzolites LS12 and LS19 show slightly depleted LREE patterns ($(La/Yb)_{Ch}$ = 0.20–0.65), comparable to the majority of cpx in lherzolites group (Fig. 6c) but at lower Heavy (H) REE and highly depleted Th and U contents (Th_{PM} = 0.08–1.18 and U_{PM} = 0.15–2.03). The cpx of this group presents ubiquitous negative Ti (Ti* = 0.17–0.42) and positive Sr (Sr* = 1.42–4.01) anomalies (Fig. 6b).

Clinopyroxene from lherzolites group has higher HREE contents (Yb_{Ch} = 8.34–11.48) than cpx-poor lherzolites with homogenously flat profiles, which evolve from highly depleted (LS09-LS05) to slightly enriched (LS20), with $(La/Yb)_{Ch}$ ratios ranging between 0.04 and 4.42 (Fig. 7c). The LREE highly depleted cpx are associated with the general depletion trend of the most incompatible elements and feeble Zr and Ti negative anomalies (Zr* = 0.25–0.59; Ti* = 0.54–0.56). The progressive LREE increase is accompanied by remarkable Th, U enrichments and variable Sr contents (Sr* = 0.64–2.31).

The cpx-rich lherzolites group is characterized by flat HREE and Middle (M) REE, $((Sm/Yb)_{Ch}$ = 0.79–1.02), with Yb_{Ch} contents ranging from 10.51 to 13.04 and a regularly decrease from Sm to La (La_{Ch} = 4.7–5.1), with the LS31 cpx showing the steepest decrease (La_{Ch} = 1.39). The cpx of this group contain systematically low Th and U contents always lower than the PM reference value, weak Ti negative anomaly Ti* = 0.52–0.6 and negligible Zr negative and Sr positive anomalies.

4.2. Mineral equilibrium, temperature, oxygen fugacity and water content estimates

The LS peridotites are texturally well equilibrated with grain boundaries slightly curved or with 120° triple junctions, geometry of

Table 2
Trace element concentrations in ppm for clinopyroxenes of Lianshan peridotite samples.

Sample	LS16	1σ	LS26	1σ	LS03	1σ	LS12	1σ	LS15	1σ	LS17	1σ	LS19	1σ	LS21
Rock type	hz				cpx-poor lh										
n.	5		5		6		5		5		4		8		6
Ba	0.072	0.084	0.089	0.045	0.071	0.068	0.023	0.002	1.881	3.136	8.596	#####	0.186	0.189	0.518
Th	1.206	0.150	0.010	0.003	0.580	0.055	0.007	0.006	4.689	0.380	4.263	0.542	0.100	0.031	1.205
U	0.401	0.042	0.002	b	0.177	0.016	0.006	0.006	0.569	0.051	0.505	0.058	0.043	0.022	0.398
Nb	0.124	0.021	0.064	0.013	0.790	0.089	0.137	0.024	0.251	0.079	0.242	0.030	0.217	0.030	0.177
Ta	0.067	0.019	0.010	0.004	0.002	0.003	0.012	0.008	0.023	0.012	0.013	0.004	0.016	0.007	0.077
La	10.39	0.27	0.34	0.03	3.92	0.90	0.27	0.04	12.96	6.61	10.81	3.46	0.95	0.21	11.60
Ce	22.69	1.22	0.84	0.04	4.64	1.40	0.97	0.03	15.98	7.73	13.17	1.87	2.21	0.38	28.16
Pr	2.493	0.179	0.119	0.020	0.391	0.093	0.189	0.014	1.481	0.393	1.368	0.066	0.346	0.048	3.408
Sr	319.3	15.6	14.9	0.9	109.7	24.1	63.1	0.7	223.9	171.6	172.4	75.3	47.7	1.1	339.0
Nd	9.91	0.68	0.64	0.07	1.60	0.25	1.16	0.14	5.03	1.02	5.20	0.27	2.03	0.11	13.90
Zr	41.6	1.0	1.9	0.2	4.2	0.2	2.5	0.1	45.5	3.0	41.6	1.4	23.1	0.6	38.7
Hf	1.088	0.099	0.057	0.028	0.186	0.047	0.133	0.024	1.147	0.204	1.018	0.062	0.620	0.048	0.872
Sm	1.891	0.132	0.165	0.035	0.539	0.080	0.489	0.032	0.837	0.077	0.724	0.049	0.787	0.082	2.747
Eu	0.690	0.029	0.069	0.013	0.245	0.024	0.212	0.028	0.197	0.031	0.184	0.023	0.389	0.029	0.941
Ti	1510	40	162	13	670	35	750	17	503	11	247	5	1221	100	1033
Gd	1.69	0.08	0.22	0.02	0.96	0.12	0.93	0.12	0.58	0.09	0.60	0.07	1.26	0.07	2.27
Tb	0.241	0.027	0.034	0.006	0.178	0.019	0.190	0.017	0.093	0.010	0.088	0.018	0.243	0.012	0.322
Dy	1.38	0.06	0.25	0.04	1.34	0.12	1.43	0.10	0.62	0.10	0.60	0.02	1.68	0.12	1.61
Y	7.0	0.1	1.6	0.1	8.0	0.1	8.8	0.1	3.4	0.1	3.4	0.1	10.1	0.3	8.1
Ho	0.272	0.020	0.061	0.009	0.308	0.012	0.328	0.013	0.135	0.009	0.130	0.020	0.386	0.024	0.307
Er	0.687	0.017	0.166	0.023	0.839	0.095	1.004	0.043	0.378	0.045	0.366	0.009	1.129	0.033	0.769
Tm	0.093	0.004	0.038	0.006	0.125	0.004	0.149	0.003	0.069	0.006	0.063	0.006	0.155	0.006	0.101
Yb	0.688	0.062	0.305	0.045	0.864	0.078	0.964	0.059	0.494	0.065	0.511	0.023	1.050	0.089	0.720
Lu	0.103	0.004	0.048	0.006	0.111	0.009	0.133	0.011	0.088	0.010	0.084	0.009	0.163	0.009	0.118

Sample	1σ	LS01	1σ	LS05	1σ	LS06	1σ	LS08	1σ	LS09	1σ	LS20	1σ	LS22	1σ
Rock type		lh													
n.		5		10		4		10		7		4		9	
Ba	0.339	0.041	0.018	0.121	0.075	0.125	b	0.260	0.178	0.786	1.334	0.031	b	0.254	0.320
Th	0.081	0.048	0.014	0.004	0.003	0.015	0.009	0.499	0.210	0.002	b	0.744	0.040	0.060	0.011
U	0.052	0.020	0.009	0.018	0.018	b.d.		0.286	0.363	b.d.		0.183	0.028	0.014	0.009
Nb	0.080	0.318	0.030	0.022	0.009	0.106	0.029	0.176	0.109	0.010	b	0.000	0.067	0.149	0.028
Ta	0.033	0.027	0.011	0.004	0.004	0.020	0.015	0.025	0.029	0.002		0.090	0.023	0.059	0.010
La	0.76	0.97	0.05	0.12	0.02	1.13	0.04	2.85	1.93	0.04	0.01	8.98	0.12	3.24	0.24
Ce	2.84	3.03	0.22	0.88	0.09	4.08	0.12	4.80	3.13	0.13	0.02	20.80	0.30	10.36	0.34
Pr	0.495	0.534	0.034	0.267	0.033	0.711	0.029	0.646	0.189	0.031	0.008	2.696	0.088	1.757	0.063
Sr	56.4	60.3	1.5	27.0	2.6	77.0	1.3	119.0	60.7	3.3	0.6	210.3	0.8	91.3	2.0
Nd	2.23	3.37	0.23	2.19	0.25	4.26	0.11	3.45	0.39	0.31	0.03	12.28	0.47	9.55	0.44
Zr	1.4	23.7	0.3	14.6	1.6	32.4	0.7	25.7	8.5	1.5	0.1	45.8	21.3	38.2	0.6
Hf	0.078	0.709	0.078	0.648	0.113	0.983	0.095	0.778	0.233	0.118	0.017	0.639	0.101	1.279	0.070
Sm	0.373	1.501	0.112	1.252	0.217	1.773	0.118	1.429	0.170	0.389	0.051	2.937	0.278	2.916	0.150
Eu	0.154	0.584	0.056	0.572	0.044	0.666	0.068	0.584	0.073	0.197	0.025	1.052	0.075	1.098	0.051
Ti	58	2465	51	2590	131	2853	33	2398	87	994	33	1474	12	4325	152
Gd	0.25	2.27	0.19	2.27	0.30	2.39	0.07	2.12	0.12	0.98	0.08	2.92	0.18	3.53	0.26
Tb	0.014	0.423	0.018	0.450	0.054	0.437	0.029	0.395	0.038	0.233	0.030	0.493	0.020	0.582	0.036
Dy	0.08	2.91	0.05	3.18	0.43	3.09	0.16	2.70	0.28	1.81	0.05	2.85	0.24	3.72	0.13

(*continued on next page*)

Table 2 (*continued*)

Sample	1σ	LS01	1σ	LS05	1σ	LS06	1σ	LS08	1σ	LS09	1σ	LS20	1σ	LS22	1σ
Y	0.6	16.2	0.3	18.3	1.8	17.2	0.5	15.4	0.8	11.9	0.3	14.6	0.5	20.5	0.5
Ho	0.017	0.656	0.043	0.730	0.086	0.675	0.033	0.633	0.052	0.416	0.039	0.576	0.036	0.795	0.037
Er	0.036	1.810	0.068	2.064	0.290	1.812	0.107	1.706	0.181	1.366	0.090	1.445	0.052	2.138	0.148
Tm	0.010	0.263	0.009	0.300	0.042	0.265	0.018	0.251	0.024	0.204	0.013	0.209	0.008	0.304	0.012
Yb	0.081	1.673	0.063	2.039	0.291	1.737	0.042	1.627	0.097	1.403	0.142	1.459	0.073	1.979	0.117
Lu	0.021	0.242	0.005	0.281	0.038	0.247	0.013	0.235	0.022	0.212	0.013	0.211	0.012	0.292	0.021

Sample	LS30	1σ	LS04	1σ	LS07	1σ	LS23	1σ	LS24	1σ	LS31	1σ
Rock type	lh		cpx-rich lh									
n.	11		7		6		4		12		11	
Ba	0.731	0.374	0.058	0.003	0.049	0.025	0.055	0.047	0.814	0.422	1.044	0.622
Th	0.201	0.071	0.015	0.009	0.011	0.007	0.015	0.009	0.017	0.009	0.034	0.050
U	0.072	0.041	0.021	b	b.d.		b.d.		0.022	0.018	0.010	0.006
Nb	0.182	0.032	0.118	0.037	0.119	0.031	0.109	0.019	0.080	0.029	0.073	0.059
Ta	0.012	0.006	0.017	0.013	0.006	0.006	0.013	0.005	0.014	0.010	0.006	0.003
La	1.37	0.44	1.08	0.06	1.11	0.06	1.18	0.04	1.23	0.05	0.33	0.04
Ce	2.85	0.32	4.01	0.10	4.13	0.11	4.27	0.03	4.46	0.24	1.77	0.21
Pr	0.487	0.020	0.714	0.030	0.736	0.016	0.770	0.018	0.803	0.035	0.429	0.039
Sr	68.9	7.4	81.9	1.0	79.0	0.9	84.5	1.2	85.2	2.5	55.4	3.6
Nd	3.26	0.34	4.48	0.27	4.42	0.15	4.65	0.26	4.96	0.35	3.30	0.30
Zr	24.3	0.6	35.0	0.7	33.8	1.2	34.1	0.6	35.2	1.0	27.6	1.1
Hf	0.787	0.053	1.105	0.072	1.026	0.117	0.964	0.089	1.087	0.107	0.987	0.167
Sm	1.290	0.133	1.860	0.060	1.784	0.108	1.818	0.190	1.901	0.157	1.579	0.171
Eu	0.585	0.041	0.762	0.015	0.728	0.036	0.766	0.064	0.787	0.048	0.726	0.092
Ti	2460	51	3498	22	2882	66	3554	77	3554	133	3110	84
Gd	2.09	0.11	2.70	0.08	2.47	0.13	2.73	0.13	2.68	0.18	2.76	0.40
Tb	0.404	0.024	0.500	0.017	0.453	0.025	0.498	0.008	0.499	0.032	0.500	0.046
Dy	2.93	0.18	3.44	0.10	3.10	0.10	3.38	0.09	3.39	0.16	3.61	0.32
Y	16.7	0.2	19.5	0.4	17.6	0.7	19.1	0.4	19.5	0.4	20.3	0.5
Ho	0.652	0.025	0.754	0.035	0.662	0.025	0.728	0.010	0.764	0.042	0.806	0.052
Er	1.845	0.088	2.099	0.074	1.920	0.088	2.078	0.059	2.142	0.113	2.210	0.198
Tm	0.263	0.020	0.306	0.012	0.268	0.010	0.302	0.008	0.313	0.025	0.327	0.037
Yb	1.718	0.109	2.027	0.103	1.787	0.094	1.992	0.064	2.072	0.116	2.217	0.272
Lu	0.252	0.024	0.285	0.015	0.253	0.019	0.292	0.018	0.296	0.033	0.316	0.039

Rock type as in Table 1.
n.: numbers of averaged samples when variations are within the analytical errors.
b.d.: below detection limits.
b: just one cpx available for the element average.
See text for full description.

Table 3
Parameters used for modelling original H_2O contents in bulk rocks and cpx.

Partition coefficients	ol/melt	ref	(opx/melt)*	ref	(ol/opx)**	ref	(ol/cpx)*	ref	(cpx/opx)*	ref
Kd H_2O	0.0014	2	0.018	2, 3	0.12	1	0.06	1	2	1
H_2O (wt%) of primary melts	min		max(off-craton)		max (on-craton)					
	0.68		1.5		2.6					4
Modes	Ol		Opx		Cpx		Sp			
PM	0.52		0.27		0.18		0.03			5
Melt	−0.05		0.08		0.87		0.10			6

References: 1 = Warren and Hauri (2014); 2 = Hirschmann et al. (2009); 3 = O'Leary et al. (2010); 4 = Luth (2013) and reference therein; 5 = McDonough and Sun (1995); 6 = Herzberg (2004).
* Al_2O_3 in pyrxene from 4 to 6 wt%.
** Compilation of experiment and natural samples.

Table 4
Rock and clinopyroxene water concentration in the upper mantle.

H_2O contents of primary melts (wt%)		From off-craton lithospheric mantle	0.68–1.5	
		From on-craton lithospheric mantle	2.6	
			PM	cpx
H_2O concentration of PM and cpx (ppm)	(F = 3%)	Minimum estimate	328	680
		Maximum estimate (off-craton)	722	1500
		Maximum estimate (on-craton)	923	2338
	(F = 8%)*	Minimum estimate	653	1356
		Maximum estimate (off-craton)	1440	3190
		Average	813	1813

* F = 8% PM on-craton maximum estimates has not petrological meaning.

low energy for mineral arrangement at mantle depth. The textural equilibrium was chemically tested by Fe-Mg distributions among minerals (Fig. 7), with the equilibrium lines derived from equations experimentally obtained by Brey and Köhler (1990) and Liermann and Ganguly (2003) between silicate minerals and spinel. The equilibrium lines were calculated at pressure of 20 Kbar, with T of 800, 900 and 1100 °C. Taking into account Fe/Mg equilibrium models for olivine-opx and olivine-spinel pairs, the LS cpx-rich lherzolites reflect the ideal Fe/Mg distribution at the temperature and pressure reference conditions (Fig. 7a and b). With respect to Fe/Mg opx-cpx equilibrium lines (Fig. 7c), "disequilibrium" is evident for the two harzburgite, cpx-poor lherzolites LS17 and lherzolites LS05, which lay outside the equilibrium region, towards low temperatures, with respect to the validity of the experimental formulations. Considering the different Fe-Mg diffusion rates among peridotite minerals, temperatures were calculated (pressure arbitrarily assumed as 20 Kbar) with both Brey and Köhler (1990, T_{BKN}) and O'Neill and Wall (1987), as modified by Ballhaus et al. (1991, T_{NWB}) formulae, based on Fe and Mg exchanges between opx-cpx and olivine-spinel respectively (Table 1). The results of the two methods, as expected, large T differences, generally exceeding the error of the methods (± 30 °C). Besides, the LS xenoliths coherently record increasing temperatures from cpx-poor lherzolites and harzburgite (T_{BKN} = 833–895 °C; T_{NWB} = 883–894 °C) to cpx-rich lherzolites (T_{BKN} = 829–1001 °C; T_{NWB} = 875–1004 °C).

Oxygen fugacity (fO_2) values were obtained from the equilibrium: $6Fe_2SiO_4$ (olivine) + O_2 (fluid) = Fe_3O_4 (spinel) + $3Fe_2Si_2O_6$ (opx) based on the semi-empirical oxygen barometer calibrated by Ballhaus et al. (1991), using X_{Fe} in spinel as Fe^{3+}/total R^{3+}, pressure of 20 Kbar and T_{NWB}. The intrinsic errors of the formula as well as the errors derived by the Fe^{3+} calculated by the stoichiometry of minerals are as

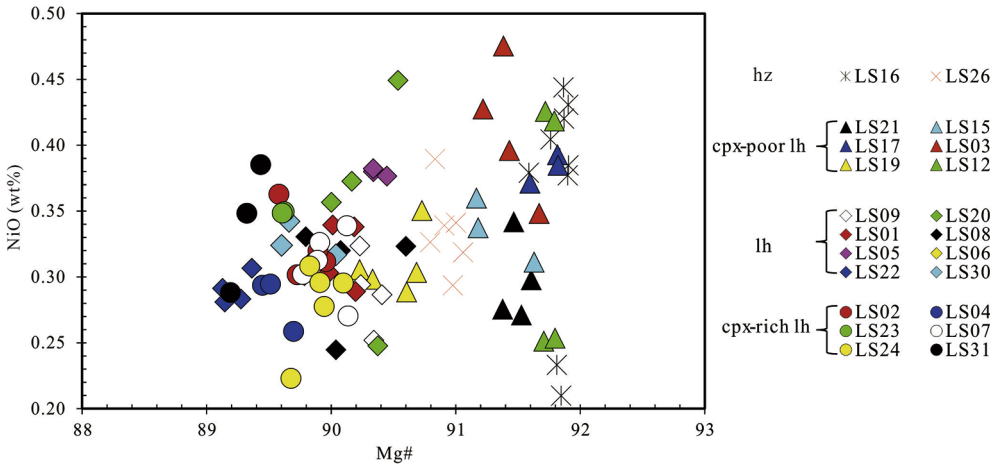

Fig. 3. Compositional variation of olivines in LS mantle xenoliths; Mg# [Mg/(Mg + Fe^{2+}) *100] versus NiO wt.% reflects, on the whole, a general positive correlation from cpx-rich lherzolites to cpx-poor lherzolites (and harzburgite).

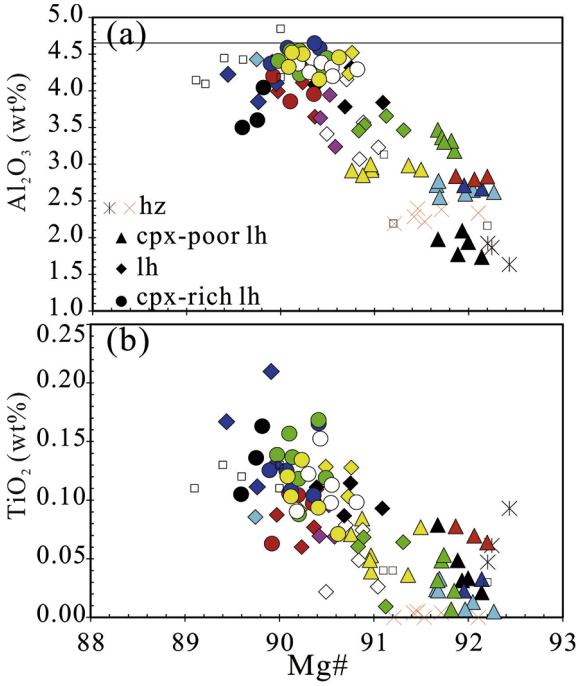

Fig. 4. Plots of Al_2O_3 (a) and TiO_2 (b) versus Mg# for orthopyroxenes. The line in (a) indicates the buffered Al_2O_3 contents for cpx-rich lherzolites group. Symbols and color code as in Fig. 3 legend; small open square: Lianshan peridotites from Lu et al. (2013).

discussed in Bonadiman et al. (2014).

The fO_2 values of LS samples, in terms of difference from the fayalite-magnetite-quartz buffer (ΔFMQ), always result below FQM buffer (ΔFMQ = −0.2 to −2.2), with the highest values recorded in the harzburgite and cpx-poor lherzolites groups (ΔFMQ range from −0.9 ± 0.7 to −1.0 ± 0.2) and the lowest values recorded in the cpx-rich lherzolites group (ΔFMQ = −1.4 ± 0.5, Table 1).

To better frame the volatile circulation in the LS mantle domain, we also reported the water contents measured in the nominally anhydrous minerals (olivine, opx and cpx) of these samples (Table 1). Detailed discussions of the data are reported in Bonadiman et al. (2009) and Xia et al. (2010). On the whole, the water contents (H_2O wt. %) in opx and cpx range from 13 to 45 ppm and from 37 to 102 ppm, respectively; it is negligible in olivine (in all samples it is always below the detection limits). In order to minimize the effect of H diffusion in ol, the partitioning between olivine, opx and cpx was used to calculate the whole-rock water contents (Bonadiman et al., 2009; Xia et al., 2010). This calculation refers to the modal contents (Table 1), and to $Kd_{H2O}^{ol/opx}$ and $Kd_{H2O}^{ol/cpx}$, based on a combination of available data from natural and experimental samples (Hauri et al., 2006; Novella et al., 2014; Tenner et al., 2009; Warren and Hauri, 2014), and assigns, as expected, the wettest lithology to the cpx-rich lherzolites (on average 22 ± 10 ppm; Table 1).

5. Discussion

5.1. Melting models

The abundance of the most fusible elements in the LS minerals systematically varies with Mg#. Such trends are usually interpreted as indicators of residues from different degrees of partial melting and melt extraction from a fertile lherzolite source.

The melting degrees (F) are provided by the major element mineral compositions following the experimental melting results in the CSMA (Fe) peridotitic system (Herzberg, 2004; Bonadiman and Coltorti, 2011). Theoretical melting curve for cpx was obtained for Si, Al, Fe, Mg

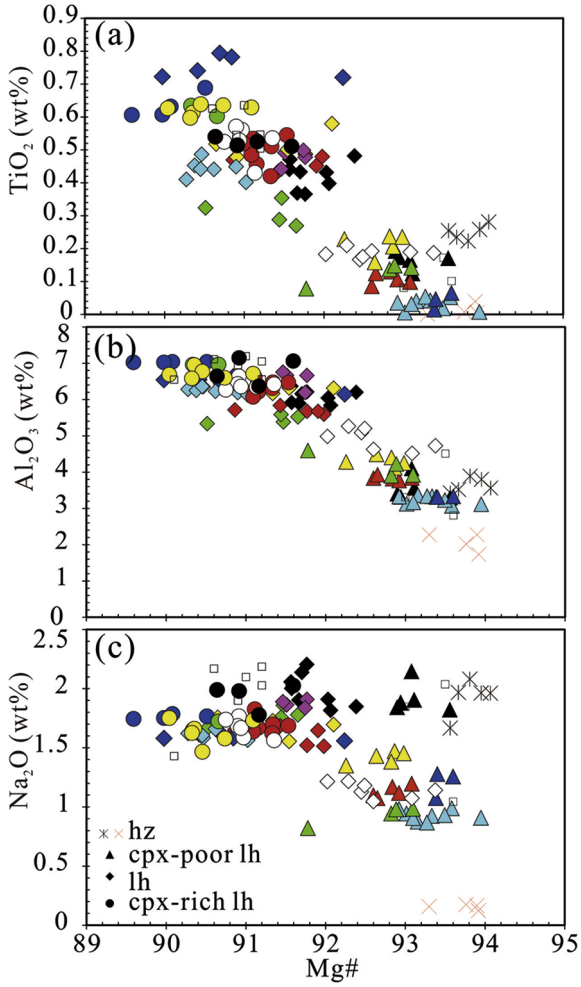

Fig. 5. Plots of TiO_2 (a), Al_2O_3 (b) and Na_2O (c) versus Mg# for clinopyroxenes. The lines in (b) and (c) indicate the buffered Al_2O_3 and Na_2O contents for cpx-rich lherzolites group. Symbols and color code as in Fig. 3 legend; small open square: Lianshan peridotites from Lu et al. (2013).

and Ca from the McDonough and Sun (1995) primitive mantle major element composition, using the mass-balance calculation between the four peridotite phases (PM bulk composition olivine:opx:cpx:spinel = 52:27:18:3) and progressive melting residua derived from the experimental results of Herzberg (2004). The curve was calculated considering the ideal basaltic melting behavior in the pressure range of the anhydrous spinel stability field (10–20 Kbar). In this model, the cpx is consumed at ~30% of PM melting. Among the basaltic elements, Al, HREE (and Y) are the most sensitive to the melting degree (Ionov and Hofmann, 2007), thus Al_2O_3 versus MgO and Yb_{PM} versus Y_{PM} were chosen to describe the melting process (Fig. 8a and b). Since a complete data set (major and trace elements) is provided for cpx only, we refer to this phase to evaluate the residual character and processes of the LS mantle domain. In Al_2O_3 versus MgO diagram LS cpx grade towards the hypothetical melting curve with the harzburgite group coherently indicating the highest melting degrees (18–24%) and lherzolites -group/cpx-rich lherzolites groups showing the lowest (4–15% and 0–9%). In the spinel stability field, the Al_2O_3 contents of cpx at the beginning of melting (F < 10%; Al_2O_3 = 7.00–6.57 wt%) are not able to clearly discriminate in the curve a reduction of modal contents from 18% (PM) to 14% melting (Fig. 8a). In fact, the whole cpx-rich lherzolites group (modal cpx = 18–14%) coherently plots in this region of the curve. On the other hand, theoretically, a rapid Al_2O_3 decrease is expected for F exceeding 10%. According to the model, the cpx of lherzolites group, with cpx modal contents confined in the range 8–14%, should reflect a

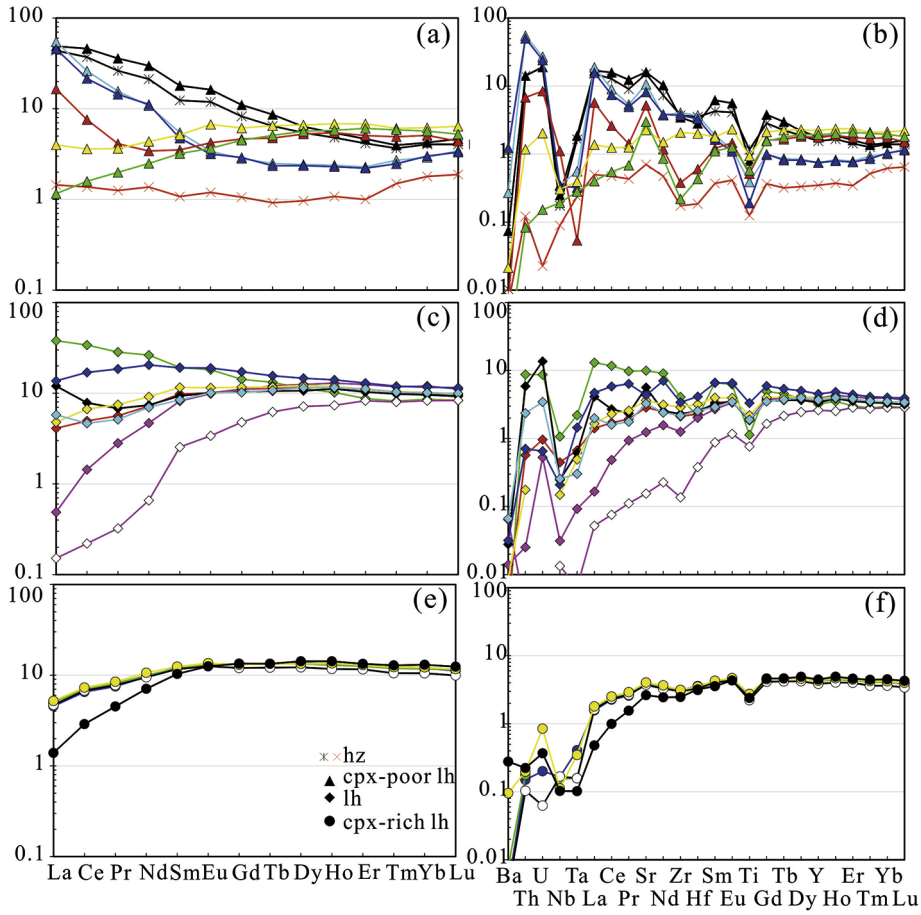

Fig. 6. REE and trace element patterns of cpx in harzburgite and cpx-poor lherzolites groups (a and b), lherzolites group (c and d) and cpx-rich lherzolites group. Chondrite and Primitive Mantle Normalization values from McDonough and Sun (1995). Symbols and color code as in Fig. 3 legend.

residuum after theoretical melting degrees between ~16 and ~12%, but they span between 15 and 4% F (Fig. 8a). The same occurs for the cpx-poor lherzolites group (cpx = 6–8% corresponding to an ideal PM melting degree in the range of ~20–22% F), which are placed in the curve between 16 and 20% F (Fig. 8a). Only LS15 and LS17 represent a residuum (F ~ 20% PM melting) coherent with the observed cpx modal contents. In this model the cpx of two harzburgites (cpx = 4%) present higher Al_2O_3 and lower MgO contents to be considered a direct melting of the PM source.

These results were compared to those obtained applying the more conventional near-fractional melting numerical model Zou (1998) to the cpx HREE (and Y) compositions (i.e. Johnson et al., 1990; Hellebrand et al., 2002; Liang and Peng, 2010) in the spinel stability field. As for the Al_2O_3-MgO model, the starting fertile cpx composition is calculated using the PM composition of McDonough and Sun (1995), cpx = 18%, and model parameters as in Bonadiman et al. (2005) and Faccini et al. (2013).

A calculation approximation to the simple ideal, fractional melting equation of Johnson et al. (1990) is applicable to ≤0.1 residual porosity (Zou, 1998). In fact, the HREE (Yb) and Y of the cpx of the entire LS suite were reproduced by the simplest fractional melting model (Fig. 8b). In agreement with the Al_2O_3-MgO melting model, the estimated degrees of partial melting for the cpx-rich lherzolites are less than 3%, leaving an estimated residue which contains a modal clinopyroxene comparable to that measured in the samples (cpx = 14–18%). LS31 represents (trace and major melting modeling) the most fertile sample of the entire collection with the cpx modal content close to PM values (18%). The model assigns to the lherzolites-group (cpx = 10–13%) a melting degree spanning between F < 3% and ~7%, slightly lower than that predicted by the Al_2O_3-MgO model. LS05 and LS22 (cpx = 13%) have Yb and Y contents close to the PM values (Fig. 8b) approaching the modal composition of the cpx-rich lherzolites group. Except for LS15 and LS17, which represent a residuum (~17% PM melting) consistent with their cpx contents (7% and 8% respectively), and analogously to what observed for the major element melting model (Fig. 8a), the cpx-poor lherzolites contain cpx with Yb and Y contents corresponding to those of a residuum after 8–13% PM melting, but the real abundance is lower than that theoretically predicted (6–8% vs. 15–12% F). The harzburgite HREE (and Y) reproduce a residuum after a maximum of 21% degree of melting of PM cpx, too low with respect to the measured cpx modal content (4%), which would suggest a F > 25%. Following the fractional melting model at 4% of modal cpx, in fact, Yb_{PM} should be as low as ~0.15–0.20 (F > 25%, rapidly approaching the cpx disappearing) with respect to the real Yb_{PM} content of LS26 (0.52–0.70).

To summarize, both the cpx major and trace element melting models, independently indicate that only cpx-rich lherzolites represent extremely fertile (close to the PM) mantle fragments fitting with the proper lithotypes (i.e. cpx modal contents).

Applying the same melting models (major and trace) to the cpx of Lu et al. (2013) xenoliths, it is evident that for all their studied samples the residual character was modified by enrichment events (Fig. 8a). In particular, cpx modal contents vs. Al_2O_3 and Y (and Yb) contents cannot be explained by any melting model, including the one proposed by the authors (Hellebrand et al., 2002). These peridotites may have been metasomatized, and resemble the lherzolites and cpx-poor lherzolites groups of our xenolith collection.

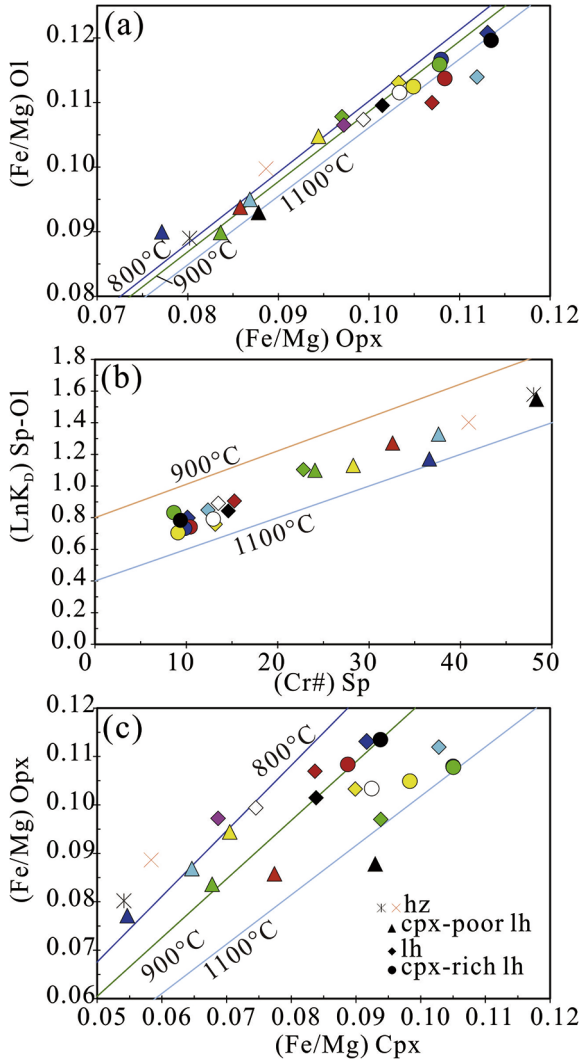

Fig. 7. Fe/Mg equilibrium diagrams for olivine vs opx (a), olivine vs. spinel (b) and opx vs. cpx (c). In (a) and (c) the equilibrium lines are from Brey & Köhler (1990) at 800, 900 and 1100 °C. In (b) K_DSpinel-Olivine is Fe-Mg partitioning between olivine and spinel determined on the basis of the Liermann and Ganguly (2003) model. (Fe/Mg) indicates Fe^{2+}/Mg, as calculated by stoichiometry for each mineral. Symbols and color code as in Fig. 3 legend.

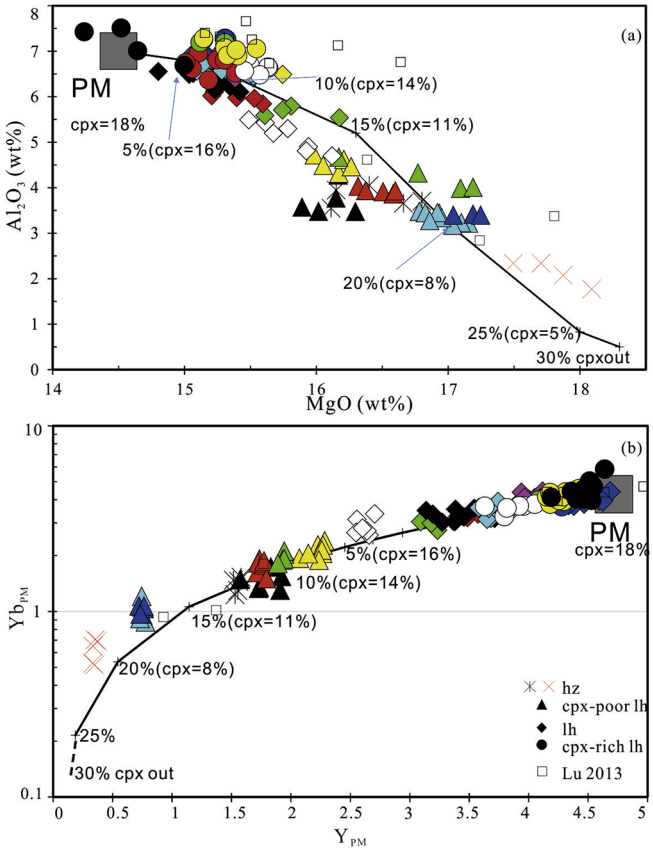

Fig. 8. Clinopyroxene Al_2O_3 vs. MgO (a) and Y and Yb contents (b) compare to calculated melting models in LS peridotitic samples. In (a) the Al_2O_3 and MgO contents of PM were calculated based on the McDonough and Sun (1995) mantle model. Model parameters as in Bonadiman et al. (2005) and Faccini et al. (2013). In (b) fractional melting model within spinel stability field based on Zou (1998). See text for further explanation. Tick marks on curves indicate partial melting percentages (F), numbers in brackets are ideal cpx modal contents at F. Symbols and color code as in Fig. 3 legend.

5.2. Metasomatism

As shown in the previous section, most of the clinopyroxenes of lherzolites, cpx-poor lherzolites and harzburgite reflect anomalous Al_2O_3 and REE enrichments with respect to the contents theoretically expected for residual cpx according to the melting models (Fig. 8). In terms of Refractory Lithophile Element (RLE), the high LREE, Th, and U contents, coupled with variable Sr enrichments of cpx in these lithotypes (Fig. 6), indicate that a variably depleted mantle sector interacted with metasomatic melts. Lu et al. (2013) report abundant CO_2 fluid inclusions in spongy cpx, which present convex-down REE patterns and high contents of highly compatible elements (Th, U, Sr and LREE). The authors argue that a refractory mantle system interacted with silicate- to carbonatitic-melt/s at the time of the host basalt entrapment. In our sample collection the absence of carbonate, hydrous mineral phases (i.e. mica, amphibole or apatite), as well as metasomatic textures (i.e. spongy and/or secondary crystals, and/or glassy patches), rules out melt circulation at depth during, or before, the host basalt eruption (Coltorti et al., 1999; Ionov et al., 2002). Since no modal metasomatic minerals were observed and all lherzolites, cpx-poor (and harzburgite) lithotypes are texturally well equilibrated, the geochemistry (major and trace elements) of clinopyroxenes is the solely indicator of the metasomatic event(s) occurred in the LS mantle domains. Trace element patterns of hypothetical liquids in instantaneous equilibrium with the most enriched cpx (harzburgite and cpx-poor lherzolites) were calculated with $D^{cpx/melt}$ using the partition coefficients of Ionov et al. (2002). The theoretical compositions reflect the imprinting of the circulating melt, since in this xenolith population cpx is the sole mineral that can accommodate the incoming trace element budget (Fig. 9). The resulting melts do not show any correspondence with the compositional range of basalts from the region (Chung 1999; Zou et al., 2000), in particular regarding the remarkable Nb (and Ta) and Ti negative anomalies that were not observed in the Subei Basin basalts (Fig. 9).

5.3. Modeling the original water contents

Under the assumption that the Earth has a chondritic RLE composition and that the H in the PM is associated with O in hydroxyl (OH) in minerals or, in minor amounts, in the form of structurally bound water molecules (H_2O) (e.g. McDonough and Sun, 1995; Lodders, 2003; Drake and Righter, 2002; Kleppe and Jephcoat, 2006), the PM total abundance of H_2O is estimated in the range of 850–1100 ppm wt. (Mottl et al., 2007; Palme and O'Neill, 2003). These values were determined by considering the hydrosphere (oceans, pore water in sediments and ice; 1.6×10^{21} kg) as the water originally contained in the 50% degassed mantle (Mottl et al., 2007) and a subsequent ingassing

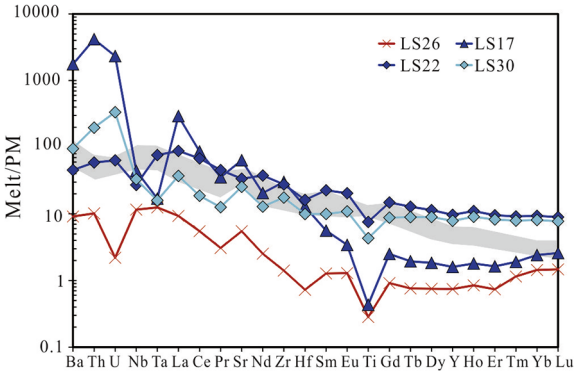

Fig. 9. Plot of PM-normalized incompatible trace element patterns for the calculated instantaneous equilibrium melts. Basalts from Subei basin (Chung, 1999 and Zou, 2000) are plotted for comparison.

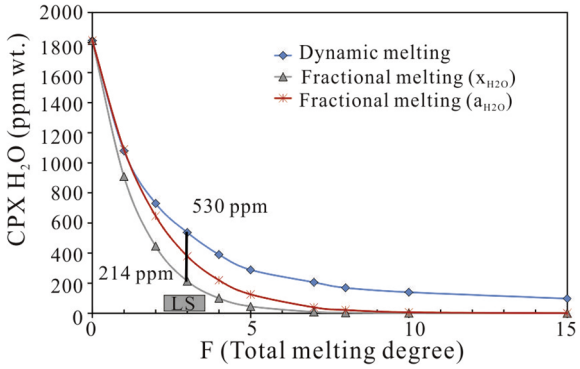

Fig. 10. Comparison of LS cpx H_2O contents (grey box) with the ideal cpx H_2O contents as residuum after 3% PM pure fractional (composition (X) and activity (a) distribution coefficient models) and dynamic (close to batch for F < 2%) melting models. At F = 3% (melting degree estimated for cpx-rich lherzolites), theoretical residuum cpx should contain H_2O in the range of 214–530 ppm. See text for further explanations.

contribution by the recycled crust into the mantle (ca. 200 ppm; Hirschmann, 2006), since the beginning of the Earth's evolution (Palme and O'Neill, 2003; Arevalo et al., 2009). Alternatively, for a non-chondritic Earth's model (i.e. O'Neill and Palme, 2008), which estimates that K abundances in the mantle were only about half of that expected from the chondritic model, ^{40}Ar (as mainly derived by ^{40}K) in the atmosphere would correspond to degassing of the entire mantle, not just 50% of it. Consequently, the PM water abundance would be 425–675 ppm, including the contribution of the recycled crust in the mantle (Palme and O'Neill, 2003).

A quantitative insight into the mantle H_2O contents may also be obtained by measuring the water contents in mantle-derived magmas. This approach would immediately confine the discussion to the Earth's upper mantle, but if referring to the whole mantle convection, it can ultimately reflect the PM water contents. Taking into account the intraplate mantle-derived melts in both oceanic and continental settings, the water contents range from 0.05 to 1.60 wt% and from 1.50 to 2.60 wt%, respectively (Luth, 2014; White and Klein, 2014 and references therein). These values do not include volatile-rich silicate magmas such as kimberlites (H_2O = 5–12 wt%) and lamprophyres (H_2O = 5–7 wt%), which are far from being the most common upper mantle derived melts (Kavanagh and Sparks, 2009; Luth, 2014 and reference therein). In our modelling we consider that 0.68–1.50 wt% could be a reasonable range of water contents in primitive mantle-derived melts; 2.60 wt% is indicated as the value representing the water contents of primary melts from on-craton lithospheric mantle (Peslier et al., 2012; Doucet et al., 2014). Based on experimentally determined H_2O partition coefficients between mantle minerals and basic melts (Table 3; Hirschmann et al., 2009; O'Leary et al., 2010), and referring to the PM mineral proportions as described in "Section 5.1 Melting models" we can roughly estimate that the water contents of a fertile mantle, close in composition to the PM, are in the range 328–1440 ppm (Table 4). This range is obtained assuming that the PM source produced alkaline primitive magmas at partial melting degree (F) varying from 3 to 8% (Table 4). As spinel represents a negligible modal portion and contains no water, and considering the $D_{H2O}^{Min/Min}$ between olivine/opx and olivine/cpx, the cpx_{PM} has H_2O in the range of 680–3190 ppm (Table 4). This range corresponds to measured H_2O contents in both natural (H_2O = 600–960 ppm; Li et al., 2008; Wade et al., 2008) and experimental cpx (Al-bearing diopside ($Di_{70-90}CaTs_{30-10}$): H_2O = 2600–1200 ppm; Gavrilenko et al., 2010).

The calculation of H_2O contents of residual peridotite (or its cpx), determined by the application of conventional REE melting models, intrinsically has a large source of error. In fact, H_2O does not follow the same melting model as REE, as erroneously supposed, considering the relatively constant H_2O/Ce ratio in cpx (and whole rock) of mid-ocean ridge basalts (MORBs; Michael, 1995; Hauri et al., 2006; Green et al., 2010; Xia et al., 2013; Hao et al., 2014, 2016). Conversely, peridotites show a considerable range of H_2O/Ce ratios at both mineral and bulk rock levels. This discrepancy is partially due to the variable petrological models which link the mantle source to its basic melts (i.e. polybaric melting histories and fluid refertilization), but the principal source of error is due to the mineral/melt and bulk/melt H_2O partition coefficients applied (Hirschmann, 2006; Warren and Hauri, 2014). The various set of published mineral/melt H_2O partition coefficients are not always internally consistent: i.e. $D_{H2O}^{Cpx/Melt}/D_{H2O}^{Opx/Melt} \neq D^{Cpx/Opx}_{H2O}$ (Warren and Hauri, 2014). This discrepancy is likely due to the different reactivity of water in minerals during melting. In fact $D_{H2O}^{min/melt}$ also depends on the mineral composition, which changes at higher degrees of melting (Zou, 1998), thus H_2O activities are not the same as those imposed by the full peridotite assemblage as applied in the equation of Novella et al. (2014). In order to better frame the H_2O behavior of cpx during melting, we modeled the melting of the initial cpx (cpx_{PM}) using the fractional melting equation of Shaw (1970), but calculating the global distribution coefficients ($D_{H2O}^{min/melt}$ and $P_{H2O}^{min/melt}$) considering the activity model (Zou, 1998; Till et al., 2010). On the basis of major and trace (lithophile) element cpx modelling, the LS cpx-rich lherzolites correspond to a residuum after a maximum of 3% of PM fractional (≈bulk) melting in the spinel stability field. In terms of H_2O contents these cpx residua should contain H_2O in the range of 214–530 ppm, depending on the model applied (Fig. 10). The cpx H_2O contents of LS cpx-rich lherzolites (41–96 ppm) are, on average, one order of magnitude lower than those of theoretically expected at 3% F (214–530 ppm). Taking into account the measured H_2O contents in cpx from cpx-rich lherzolites, an unrealistic 7% of F would be envisaged for this lithotype (Table 1; Fig. 10).

The low to very low H_2O contents should discharge the potential hydrogen addition from the host magma. The absence of water addition to the xenolith from the host magma is coherent with the mechanism of exhumation by fast ascent of the magma (several hours/days according to estimates of alkaline magma ascent rate) leaving no time for significant exchange of water with the entrapped xenoliths. Moreover, the homogenous H_2O content within single pyroxene grains and the equilibrium H_2O partitioning between the clinopyroxene and orthopyroxene (Bonadiman et al., 2009; Xia et al., 2010) disclaim a potential H-loss during the xenolith ascent. This difference outmatches the model uncertainties, therefore the measured H_2O in cpx (at least in the center of the mineral grains) represent the H_2O contents they had in the mantle prior to sampling by the host basalt.

5.4. Heat and H diffusivities

H diffusivities in mantle minerals (ol, cpx and opx) are very high

($D = 10^{-10}$–10^{-11} m^2/s at 900 °C; Ingrin and Blanchard, 2006; Farver, 2010; Bizimis and Peslier, 2015), and mainly controlled by volume diffusion (vacancy diffusion) through the crystal lattice (Farver, 2010). In turn, cation diffusion processes mainly control the trace element (REE) abundances in olivine (and pyroxene). Cation diffusion through minerals is slow (REE in diopside: 8 log units lower than H), consequently, the solid/melt interactions (metasomatic event) would produce a chemical zoning (i.e. REE) of minerals which characterizes the solid until a new mantle process occurs. Moreover, despite the large differences in RLE contents of LS pyroxenes, the T° values from cpx-poor lherzolites (and harzburgite) to cpx-rich lherzolites, are in the narrow interval of 200 °C and never exceed 1021 °C (Table 1).

The thermal diffusivity of mantle rocks is known to remain almost constant ($D = 4–7 \times 10^{-7}$ m^2/s; Gibert et al., 2003) when measured in polycrystalline systems between 750 and 1350 °C, with local increase due to the reactive processes. The pressure dependence is expected to be low (Katsura, 1995; Gibert et al., 2003). Applying the simplest diffusion equation of Crank (1975), valid for homogeneous diffusion rate on a finite isotropic plane medium at constant diffusion coefficient, we calculated that the residuum cpx (500 μm length) after 3% of PM melting progressively loses its initial H_2O content (Co_{H2O} 214–530 ppm; Fig. 10) to reach 50 ppm (average of measured contents) in 40.000–70.000 years. If we extrapolate this punctual data to a column of mantle sector as large as the area of xenolith samples (1 Km^2), we can estimate homogenous H_2O contents (50 ppm) in a time span of 1.5–2.4 My. Taking into account the reduction of the parameters used for the calculations, these values contain large uncertainties; nevertheless, they give important information on the time scale of the dehydration process.

6. Conclusions

Within the LS xenoliths population, the cpx-rich lherzolites group shows the most fertile compositions: Mg# and NiO contents of olivine similar, on average, to the Ol_{PM} estimates (McDonough and Sun, 1995); the Al_2O_3, TiO_2 and Na_2O contents of pyroxenes and Cr# of spinel are also close to the ideal PM values. The melting degrees estimated by clinopyroxene major and trace elements are very low (always < 3%), with coherent cpx modal contents (Fig. 8). Cpx trace element and REE patterns indicate no metasomatic effects for this lithotype.

In turn, harzburgite together with cpx-poor lherzolites (and lherzolites) reflect variable enrichments superimposed on a variably depleted (8–23% of partial melting) mantle. The metasomatic event/s introduce Al_2O_3, LREE, even HREE, modifying the expected cpx/whole chemistry residual relationship. The reconstructed trace element profiles (Fig. 9) of the hypothetical metasomatic melt/s show negative Ti, Nb-Ta and positive Sr anomalies as well as Th, U high contents; this, associated with Al_2O_3 and HREE enrichments in cpx, would indicate the circulation of a silicate melt with crustal components (i.e.: Faccini et al., 2013).

The LS peridotites contain, on average, 22 ppm H_2O, with the highest values up to 30 ppm recorded in cpx-rich lherzolites. In terms of major and trace element geochemistry, LS cpx-rich lherzolites reflect a mantle domain, which does not seem to have acted as magma source, or at least it represents a residuum of < 3% of PM melting in the spinel stability field. Comparing the water contents of cpx-rich lherzolites with the PM water estimates, it is evident that, while the RLE composition (i.e. REE and Al) of this lithotype perfectly fits the PM model (Fig. 8), the H_2O contents are significantly lower than the theoretical values (Fig. 10). Water contents of LS peridotites are even lower than the mantle source (H_2O ~ 80 ppm; DMM, Workman and Hart, 2005) of the "driest" MORB (H_2O ~ 0.05 wt%; Luth, 2013). Overall, water contents of LS peridotites show no systematical variation among rock types (Table 1) and no correlation with Yb (and Y) or Al_2O_3 contents of cpx. For instance, the harzburgite LS26 and cpx-rich lherzolites LS31 have similar water contents (57 vs. 55 ppm), but they represent different mantle domains, probably adjacent at the time of basalt capturing.

On the basis of the petrology and geochemical data reported above and accordingly to what proposed by Lu et al. (2013) it is reasonable to infer that a cold highly refractory harzburgite and cpx-poor lherzolites could represent the old cratonic lithospheric mantle modified by interaction with metasomatic melts, involving crustal components. Cpx-rich lherzolites constitute fragments of upwelling cooled fertile asthenosphere after the removal/erosion of the base of the lithospheric mantle. This asthenospheric portion had higher T, lower fO_2 and higher water contents than the pristine lithosphere.

Since heat and H are the highest diffusive components (8–10 orders of magnitude higher than the highest diffusive RLE) and highly dependent on T, it would take < 5 Ma for a mantle portion about 1 km^2 in size to re-equilibrated with the surrounding old and cold lithosphere after the last partial melting episode.

Acknowledgments

We thank two anonymous reviewers and the editor for the comments and suggestions. This work was supported by the National Natural Science Foundation of China (nos. 41225005, 41672053).

Appendix A. Supplementary material

Supplementary data to this article can be found online at https://doi.org/10.1016/j.jaesx.2019.100006.

References

Arevalo, R., McDonough, W.F., Luong, M., 2009. The K/U ratio of the silicate Earth: Insights into mantle composition, structure and thermal evolution. Earth Planet. Sci. Lett. 278, 361–369.
Ballhaus, C., Berry, R.F., Green, D.H., 1991. High pressure experimental calibration of the olivine-orthopyroxene-spinel oxygen geobarometer: implications for the oxidation state of the upper mantle. Contrib. Mineral. Petrol. 107, 27–40.
Bonadiman, C., Coltorti, M., 2011. Numerical modelling for peridotite phase melting trends in the SiO_2-Al_2O_3-FeO-MgO-CaO system at 2 GPa. Mineral. Mag. 75, 548.
Bonadiman, C., Beccaluva, L., Coltorti, M., Siena, F., 2005. Kimberlite-like metasomatism and 'garnet signature' in spinel-peridotite xenoliths from Sal, Cape verde archipelago: relics of a subcontinental mantle domain within the Atlantic oceanic lithosphere? J. Petrol. 46, 2465–2493.
Bonadiman, C., Hao, Y.T., Coltorti, M., Dallai, L., Faccini, B., Huang, Y., Xia, Q.K., 2009. Water contents of pyroxenes in intraplate lithospheric mantle. Eur. J. Min. 21, 637–647.
Bonadiman, C., Nazzareni, S., Coltorti, M., Comodi, P., Giuli, G., Faccini, B., 2014. Crystal chemistry of amphiboles: implications for oxygen fugacity and water activity in lithospheric mantle beneath Victoria Land, Antarctica. Contrib. Mineral. Petrol. 167, 984.
Bizimis, M., Peslier, A.H., 2015. Water in Hawaiian garnet pyroxenites: Implications for water heterogeneity in the mantle. Chem. Geol. 397, 61–75.
Brey, G.P., Köhler, T., 1990. Geothermobarometry in four-phase lherzolites II: New thermobarometers, and practical assessment of existing thermobarometers. J. Petrol. 31, 1353–1378.
Chen, C., Liu, Y., Foley, S.F., Ducea, M.N., He, D., Hu, Z., et al., 2016. Paleo-asian oceanic slab under the north china craton revealed by carbonatites derived from subducted limestones. Geology 44 (12) e414-e414.
Chung, S.L., 1999. Trace element and isotope characteristics of Cenozoic basalts around the Tanlu fault with implications for the eastern plate boundary between North and South China. J. Geol. 107, 301–312.
Coltorti, M., Bonadiman, C., Hinton, R.W., Siena, F., Upton, B.G.J., 1999. Carbonatite metasomatism of the oceanic upper mantle: evidence from clinopyroxenes and glasses in ultramafic xenoliths of Grade Comore, Indian ocean. J. Petrol. 40, 133–165.
Craddock, P.R., Warren, J.M., Dauphas, N., 2013. Abyssal peridotites reveal the near-chondritic Fe isotopic composition of the Earth. Earth Planet. Sci. Lett. 365, 63–76.
Crank, J., 1975. The Mathematic of Diffusion. Clarendon Press, Oxford, pp. 421.
Deng, J.F., Mo, X.X., Zhao, H.L., Wu, Z.X., Luo, Z.H., Su, S.G., 2004. A new model for the dynamic evolution of Chinese lithosphere, continental roots-plume tectonics. Earth Sci. Rev. 65, 223–275.
Dick, H.J.B., Bullen, T., 1984. Chromian spinel as a petrogenetic indicator in abyssal and alpine-type peridotites and spatially associated lavas. Contrib. Mineral. Petrol. 86, 54–76.
Doucet, L.S., Peslier, A.H., Ionov, D.A., Brandon, A.D., Golovin, A.V., Goncharov, A.G., Ashchepkov, I.V., 2014. High water contents in the Siberian cratonic mantle linked to metasomatism: An FTIR study of Udachnaya peridotite xenoliths. Geochim. Cosmo. Acta 137, 159–187.
Drake, M.J., Righter, K., 2002. Determining the composition of the Earth. Nature 416, 39–44.

Faccini, B., Bonadiman, C., Coltorti, M., Gregoire, M., Siena, F., 2013. Oceanic material recycled within the sub-Patagonian lithospheric mantle (Cerro del Fraile, Argentina). J. Petrol. 54, 1211–1258.
Farver, J.R., 2010. Oxygen and hydrogen diffusion in minerals. Rev. Mineral. Geochem. 72, 447–507.
Gao, S., Rudnick, R.L., Yuan, H.L., Liu, X.M., Liu, Y.S., Xu, W.L., Ling, W.L., Ayers, J., Wang, X.C., Wang, Q.H., 2004. Recycling lower continental crust in the North China craton. Nature 432, 892–897.
Gao, S., Rudnick, R.L., Xu, W.L., Yuan, H.L., Liu, Y.S., Walker, R.J., Puchtel, I.S., Liu, X.M., Huang, H., Wang, X.R., Yang, J., 2008. Recycling deep cratonic lithosphere and generation of intraplate magmatism in the North China Craton. Earth Planet. Sci. Lett. 270, 41–53.
Gavrilenko, P., Ballaran, T.B., Keppler, H., 2010. The effect of Al and water on the compressibility of diopside. Am. Mineral. 95, 608–616.
Gibert, B., Seipold, U., Tommasi, A., Mainprice, D., 2003. Thermal diffusivity of upper mantle rocks influence of temperature pressure and the deformation fabric. J. Geoph. Res. 108 (B8), 2359. https://doi.org/10.1029/2002JB002108.
Green, D.H., Hibberson, W.O., Kovács, I., Rosenthal, A., 2010. Water and its influence on the lithosphere-asthenosphere boundary. Nature 467 (7314), 448–451.
Griffin, W.L., Andi, Z., O'Reilly, S.Y., Ryan, C.G., 1998. Phanerozoic evolution of the lithosphere beneath the Sino-Korean craton. In: Flower, M. (Ed.), Mantle Dynamics and Plate Interactions in East Asia. AGU Geodynamics Series, pp. 107–126.
Griffin, W.L., Powell, W.J., Pearson, N.J., O'Reilly, S.Y., 2008. GLITTER: data reduction software for laser ablation ICP-MS (appendix). In: Sylvester, P. (Ed.), Laser Ablation-ICP-MS in the Earth Sciences. Short Course Series. Mineralogical Association of Canada (MAC), pp. 308–311.
Griffin, W.L., O'Reilly, S.Y., Afonso, J.C., Begg, G.C., 2009. The composition and evolution of lithospheric mantle: a re-evaluation and its tectonic implications. J. Petrol. 50, 1185–1204.
Hao, Y.T., Xia, Q.K., Liu, S.C., Feng, M., Zhang, Y.P., 2012. Recognizing juvenile and relict lithospheric mantle beneath the North China Craton: Combined analysis of H_2O, major and trace elements and Sr-Nd isotope compositions of clinopyroxenes. Lithos 149, 136–145.
Hao, Y.T., Xia, Q.K., Li, Q.W., Chen, H., Feng, M., 2014. Partial melting control of water contents in the Cenozoic lithospheric mantle of the Cathaysia block of China. Chem. Geol. 380, 7–19.
Hao, Y., Xia, Q., Jia, Z., Zhao, Q., Li, P., Feng, M., et al., 2016. Regional heterogeneity in the water content of the cenozoic lithospheric mantle of eastern China. J. Geophys. Res. Solid Earth 121 (2), 517–537.
Hauri, E., Gaetani, G., Green, T., 2006. Partitioning of water during melting of the Earth's upper mantle at H2O-undersaturated conditions. Earth Planet. Sci. Lett. 248 (3–4), 715–734.
Hellebrand, E., Snow, J.E., Hoppe, P., Hofmann, A.W., 2002. Garnet-field melting and late-stage refertilization in 'residual' abyssal peridotites from the Central Indian Ridge. J. Petrol. 43, 2305–2338.
Herzberg, C., 2004. Geodynamic information in peridotite petrology. J. Petrol. 45 (12), 2507–2530.
Hirschmann, M.M., 2006. Water, melting, and the deep Earth H_2O cycle. Annual Rev. Earth Planet. Sci 34, 629–653.
Hirschmann, M.M., Tenner, T., Aubaud, C., Withers, A.C., 2009. Dehydration melting of nominally anhydrous mantle: The primacy of partitioning. Phys. Earth Planet. Inter. 176, 54–68.
Ingrin, J., Blanchard, M., 2006. Diffusion of hydrogen in minerals. Rev. Mineral. Geochem. 62, 291–320.
Ionov, D.A., Hofmann, A.W., 2007. Depth of formation of subcontinental off-craton peridotites. Earth Planet. Sci. Lett. 261, 620–634.
Ionov, D.A., Bodinier, J.L., Mukasa, S.B., Zanetti, A., 2002. Mechanism and sources of mantle metasomatism: major and trace element compositions of peridotite xenoliths form Spitzbergen in the context of numerical modelling. J. Petrol. 43, 2219–2259.
Johnson, K.T.M., Dick, H.J.B., Shimizu, N., 1990. Melting in the oceanic upper mantle: An ion microprobe study of diopsides in abyssal peridotites. J. Geoph. Res. 90, 2661–2678.
Katsura, T., 1995. Thermal diffusivity of periclase at high temperatures and high pressures. Phys. Earth Planet. Int. 101, 73–77.
Kavanagh, J.L., Sparks, R.S.J., 2009. Temperature changes in ascending kimberlite magma. Earth Planet. Sci. Lett. 286, 404–413.
Kleppe, A.K., Jephcoat, A.P., 2006. Raman spectroscopic studies of hydrous and nominally anhydrous deep mantle phases. In: Earth's Deep Water Cycle. Geophysical Monograph by the American Geophysical Union 168, pp. 69–93.
Korenaga, K., Kelemen, P.B., 2000. Major element heterogeneity in the mantle source of the North Atlantic igneous province. Earth Planet. Sci. Lett. 184, 251–268.
Li, S.G., Xiao, Y.L., Liou, D.L., Chen, Y.Z., Ge, N.G., Zhang, Z.Q., Sun, S.S., Cong, B.L., Zhang, R.Y., Hart, S.R., Wang, S.S., 1993. Collision of the North China and Yangtze Blocks and formation of coesite-bearing ecologites: Timing and process. Chem. Geol. 109, 89–111.
Li, Z.X.A., 1994. Collision between the North and South China blocks: a crustal-detachment model for suturing in the region east of the Tanlu fault. Geology 22, 739–742.
Li, Z.A., Lee, C.T.A., Peslier, A.H., Lenardic, A., Mackwell, S.J., 2008. Water contents in mantle xenoliths from the Colorado Plateau and vicinity: Implications for the mantle rheology and hydration-induced thinning of continental lithosphere. J. Geoph. Res. 113. https://doi.org/10.1029/2007JB005540.
Liang, Y., Peng, Q., 2010. Non-modal melting in an upwelling mantle column: Steady-state models with applications to REE depletion in abyssal peridotites and the dynamics of melt migration in the mantle. Geoch. Cosmochim. Acta 74, 321–339.
Liermann, H.P., Ganguly, J., 2003. Fe^{2+}- Mg fractionation between orthopyroxene and spinel: experimental calibration in the system FeO-MgO-Al_2O_3-Cr_2O_3-SiO_2, and applications. Contrib. Mineral. Petrol. 145, 217–227.
Liu, R.X., Chen, W.J., Sun, J.Z., Li, D.M., 1992. The k-Ar age and tectonic environment of Cenozoic volcanic rock in China (in Chinese) In: Liu, R.X. (Ed.), The Age and Geochemistry of Cenozoic Volcanic Rock in China. Seismologic Press, Beijing, pp. 1–43.
Lodders, K., 2003. Solar system abundances and condensation temperatures of the elements. Astroph. J. 591, 1220–1247.
Lu, J.G., Zheng, J.P., Griffin, W.L., Yu, C.M., 2013. Petrology and geochemistry of peridotite xenoliths from the Lianshan region: Nature and evolution of lithospheric mantle beneath the lower Yangtze block. Gondwana Res. 23, 161–175.
Luth, R.W., 2013. Melting in the Mg2SiO4-H2O system at 3 to 12 GPa. Geophys. Res. Lett. 20, 233–235.
Luth, R.W., 2014. Volatile in the Earth Mantle. In: Carlson, R.W. (Ed.), Treatise of Geochemistry, Vol. 3: The Mantle and Core. Elsevier, pp. 355–391.
McDonough, W.F., Sun, S.S., 1995. The composition of the Earth. Chem. Geol. 120, 223–253.
Menzies, M.A., Xu, Y.G., Zhang, H.F., Fan, W.M., 2007. Integration of geology, geophysics and geochemistry: A key to understanding the North China Craton. Lithos 96, 1–21.
Mercier, J.C.C., Nicolas, A., 1975. Texture and fabrics of upper-mantle peridotite as illustrated by xenoliths from basalts. J. Petrol. 16, 454–487.
Michael, P.J., 1995. Regionally distinctive sources of depleted MORB: Evidence from trace elements and H_2O. Earth Planet. Sci. Lett. 131, 301–320.
Mottl, M.J., Glazer, B.T., Kaiser, R.I., Meech, K.J., 2007. Water and astrobiology. Chemie der Erde 67, 253–282.
Mysen, B., 1978. Experimental determination of nickel partition coefficients between liquid, pargasite and parent peridotite minerals and concentration limits of behavior according to Henry's Law at high pressure and temperature. Am. J. Sci. 278, 217–243.
Novella, D., Frost, D.J., Hauri, E.H., Bureau, H., Raepsaet, C., Roberge, M., 2014. The distribution of H_2O between silicate melt and nominally anhydrous peridotite and the onset of hydrous melting in the deep upper mantle. Earth Planet. Sci. Lett. 400, 1–13.
O'Leary, J.A., Gaetani, G.A., Hauri, E.H., 2010. The effect of tetrahedral Al^{3+} on the partitioning of water between clinopyroxene and silicate melt. Earth Planet. Sci. Lett. 297, 111–120.
O'Neill, H.S.C., Wall, V.J., 1987. The olivine-orthopyroxene-spinel oxygen geobarometer, the nickel precipitation curve, and the oxygen fugacity of the Earth's upper mantle. J. Petrol. 28, 1169–1191.
O'Neill, H.S.C., Palme, H., 2008. Collisional erosion and the non-chondritic composition of the terrestrial planets. Philosph. Trans. Royal Soc. Series A 366, 4205–4238.
Palme, H., O'Neill, H.S.C., 2003. Cosmochemical estimates of mantle composition. In: Carlson, R.W. (Ed.), Treatise on Geochemistry vol. 2: The Mantle and Core. Elsevier, pp. 1–38.
Peslier, A.H., Woodland, A.B., Bell, D.R., Lazarov, M., Lapen, T.J., 2012. Metasomatic control of water contents in the Kaapvaal cratonic mantle. Geochim. Cosmochim. Acta 97, 213–246.
Reisberg, L., Zhi, X.C., Lornand, J.P., Wagner, C., Peng, Z.C., Zimmermann, C., 2005. Re-Os and S systematics of spinel peridotite xenoliths from east central China: Evidence for contrasting effect of melt percolation. Earth Planet. Sci. Lett. 139, 286–308.
Rudnick, R.L., Gao, S., Ling, W.L., Liu, Y.S., McDonough, W.F., 2004. Petrology and geochemistry of spinel peridoite xenoliths from Hannuoba and Qixia, North china Craton. Lithos 77, 609–637.
Shao, J.J., Huang, J.L., Yan, Z.Y., Liu, Z.P., 1989. The division and age of basalts in the Nanjing area. Geol. Rev. 35, 97–106 (in Chinese).
Shaw, D.M., 1970. Trace element fractionation during anataxis. Geochim. Cosmochim. Acta 34, 237–243.
Su, Y.P., Zheng, J.P., Griffin, W.L., Zhao, J.H., O'Reilly, S.Y., Tang, H.Y., Ping, X.Q., Xiong, Q., 2013. Petrogenesis and geochronology of Cretaceous adakitic, I- and A-type granitoids in the NE Yangtze block: Constraints on the eastern subsurface boundary between the North and South China blocks. Lithos 175–176, 333–350.
Tang, Y.J., Zhang, H.F., Ying, J.F., Su, B.X., Chu, Z.Y., Xiao, Y., Zhao, X.M., 2013. Highly heterogeneous lithospheric mantle beneath the Central Zone of the North China Craton evolved from Archean mantle through diverse melt refertilization. Gondwana Res. 23, 130–140.
Tenner, T.J., Hirschmann, M.M., Withers, A.C., Hervig, R.L., 2009. Hydrogen partitioning between nominally anhydrous upper mantle minerals and melt between 3 and 5 GPa and applications to hydrous peridotite partial melting. Chem. Geol. 262 (1–2), 42–56.
Till, C.B., Elkins-Tanton, L.T., Fischer, K.M., 2010. A mechanism for low-extent melts at the lithosphere-asthenosphere boundary. G3 (Geochem. Geophys. Geosyst.) 11, Q10015. https://doi.org/10.1029/2010GC003234.
Wade, J.A., Plank, T., Hauri, E.H., Kelley, K.A., Roggensack, K., Zimmer, M., 2008. Prediction of magmatic water contents via measurement of H_2O in clinopyroxene phenocrysts. Geology 36, 799–802.
Warren, J.M., Hauri, E.H., 2014. Pyroxenes as tracers of mantle water variations. J. Geoph. Res.: Solid Earth 119, 1851–1881.
White, W.M., Klein, E.M., 2014. Composition of the oceanic crust. In: Rudnik, R. (Ed.), Treatise on Geochemistry, vol. 4: The Crust. Elsevier, pp. 457–496.
Windley, B.F., Maruyama, S., Xiao, W.J., 2010. Delamination/thinning of sub-continental lithospheric mantle under Eastern China: The role of water and multiple subduction. Am. J. Sc. 310, 1250–1293.
Workman, R.K., Hart, S.R., 2005. Major and trace element composition of the depleted MORB mantle (DMM). Earth Planet. Sci. Lett. 231, 53–72.
Wu, F.Y., Walker, R.J., Yang, Y.H., Yuan, H.L., Yang, J.H., 2006. The chemical-temporal evolution of lithospheric mantle underlying the North China Craton. Geochim. Cosmochim. Acta 70, 5013–5034.
Wu, K., Ling, M.X., Sun, W., Guo, J., Zhang, C.C., 2017. Major transition of continental basalts in the early cretaceous: implications for the destruction of the north china

craton. Chem. Geol. 470.
Xia, Q.K., Hao, Y.T., Li, P., Deloule, E., Coltorti, M., Dallai, L., Yang, X.Z., Feng, M., 2010. Low water content of the Cenozoic lithospheric mantle beneath the eastern part of the North China Craton. J. Geoph. Res. 115. https://doi.org/10.1029/2009JB006694.
Xia, Q.K., Hao, Y.T., Liu, S.C., Gu, X.Y., Feng, M., 2013. Water contents of the Cenozoic lithospheric mantle beneath the western part of the North China Craton: Peridotite xenolith constraints. Gondwana Res. 23, 108–118.
Xu, X.S., Griffin, W.L., O'Reilly, S.Y., Pearson, N.J., Geng, H.Y., Zheng, J.P., 2008. Re-Os isotopes of sulfides in mantle xenoliths from eastern China: Progressive modification of lithospheric mantle. Lithos 102, 43–64.
Xu, Y.G., 2001. Thermo-tectonic destruction of the Archean lithospheric keel beneath the Sino-Korean Craton in China: evidence, timing and mechanism. Phys. Chem. Earth 26, 747–757.
Ying, J.F., Zhang, H.F., Tang, Y.J., Su, B.X., Zhou, X.H., 2013. Diverse crustal components in pyroxenite xenoliths from Junan, Sulu orogenic belt: Implications for lithospheric modification invoked by continental subduction. Chem. Geol. 356, 181–192.
Zhang, H.F., Sun, M., Zhou, X.H., Zhou, M.F., Fan, W.M., Zheng, J.P., 2003. Secular evolution of the lithosphere beneath the eastern North China Craton: evidence from Mesozoic basalts and high-Mg andesites. Geochim. Cosmochim. Acta 67, 4373–4387.
Zhu, G., Liu, G.S., Niu, M.L., Xie, C.L., Wang, Y.S., Xiang, B.W., 2009. Syn-collisional transform faulting of the Tan-Lu fault zone, East China. Intern. J. Earth Sci. 98, 135–155.
Zou, H.B., 1998. Trace element fractionation during modal and nonmodal dynamic melting and open-system melting: A mathematical treatment. Geochim. Cosmochim. Acta 62, 1937–1945.
Zou, H., Zindler, A., Xu, X., Qi, Q., 2000. Major, trace element, and Nd, Sr and Pb isotope studies of Cenozoic basalts in SE China: mantle sources, regional variations, and tectonic significance. Chem. Geol. 171, 33–47.